PHYSICAL REVIEW B **108**, 235420 (2023)

Large contributions from optical phonons to thermal transport in hexagonal carbon-boron-nitrogen monolayers

Xue-Kun Chen (陈学坤),[1] Yue Zhang (张越),[1] Qing-Qing Luo (罗青清),[1] Xue Chen (陈雪),[1]
Pin-Zhen Jia (贾聘真),[2,*] and Wu-Xing Zhou (周五星)[3,†]
[1]*School of Mathematics and Physics and Hunan Key Laboratory of Mathematical Modeling and Scientific Computing, University of South China, Hengyang 421001, China*
[2]*Department of Mathematics and Physics, Hunan Institute of Technology, Hengyang 421002, China*
[3]*School of Materials Science and Engineering and Hunan Provincial Key Laboratory of Advanced Materials for New Energy Storage and Conversion, Hunan University of Science and Technology, Xiangtan 411201, People's Republic of China*

(Received 21 August 2023; revised 1 November 2023; accepted 14 November 2023; published 13 December 2023)

As representative semiconducting hexagonal carbon-boron-nitride lattices, C_6BN and C_2BN are experimentally realized two-dimensional (2D) plane materials and have recently become the focus of research. Herein, combining first-principles calculations with the Boltzmann transport equation, we performed a comprehensive study on the phonon interaction and thermal conductivity in C_6BN and C_2BN monolayers. It is found that the thermal conductivities of C_6BN and C_2BN monolayers at room temperature are reduced by 79% and 73%, respectively, due to four-phonon scattering, compared with the results including three-phonon scattering only. We can attribute this phenomenon to giant four-phonon scattering exclusive for the heat-carrying out-of-plane acoustic (ZA) phonons, because the reflection symmetry allows four-ZA processes much higher than three-ZA processes, and the quasiparallel behavior between the ZA and low-lying out-of-plane optical (ZO) branches contribute to a broad phase space for four-phonon scattering as well. Moreover, C_6BN monolayer exhibits unusual behavior that optical phonons contribute about ~60% to the overall thermal conductivity under the four-phonon picture, which differs from the traditional case that acoustic phonons dominate thermal conductivity. Unexpectedly, two low-lying ZO modes have as high as 38% contributions to the thermal transport at 300 K under the four-phonon picture, causing 60% contribution of optical phonon modes, apparently larger than that of the three-phonon case (15%) and many other 2D materials, also indicating the four-phonon scattering has a more significant effect on acoustic phonons than on optical phonons. This finding not only highlights insight into the nature of phonon transport, but also provides a promising strategy for manipulation of heat transport based on optical phonon modes.

DOI: 10.1103/PhysRevB.108.235420

I. INTRODUCTION

Graphene, a planar honeycomb lattice of carbon atoms, possesses excellent carrier mobility, large stretchability, superior optical transparency, and ultrahigh thermal conductivity [1–4], which promote the use of this novel material for the design of a wide variety of advanced devices. However, the zero-gap nature of graphene limits its effective application in semiconductor devices such as field-effect transistors, gas sensors, and energy conversion, where a suitable gap in the band structure is a critical factor for obtaining good device performance. The drawback of graphene has stimulated the prediction and synthesis of the isomorphic semiconductors [5,6]. In this regard, it is worth mentioning that hexagonal boron nitride (h-BN), called "white graphene" for its honeycomb lattice arranged by alternating boron and nitrogen atoms, is experimentally demonstrated to exhibit a large direct bandgap of 5.9 eV [7]. Obviously, h-BN cannot directly be applied in semiconductor electronics and optoelectronics in which a direct and narrow bandgap is essential. Although graphene and h-BN show contrasting electronic properties, both have closely matched lattices, and excellent thermal and mechanical responses. Hence, it is natural to wonder what would happened if the ternary compounds composed of carbon, boron, and nitrogen atoms are constructed utilizing the hexagonal atomic lattice as a foundation ($h-C_xB_yN_z$), which could potentially overcome the limitations of individual structures and open up a wide range of properties and applications. In fact, some theoretical calculations and experimental results suggested that the major advantages of the $h-C_xB_yN_z$ lattices are their composition and arrangement diversities that could translate into greater freedom to modulate the physical properties [8–11]. For instance, Ci *et al.* [8] reported that the electrical conductivities of $h-C_xB_yN_z$ ribbons increase with the increase of the atomic percentage of C, promoting bandgap-engineered applications in semiconducting electronics. In addition, kınacı *et al.* [10] demonstrated that the thermal conductivity of $h-C_xB_yN_z$ structure can be widely tuned by composition and chemical design. Lately, a C-rich $h-C_xB_yN_z$ layered structure, C_6BN nanosheets, have been already fabricated by a convenient two-step borylation reaction [12,13], and theoretical results confirm that the C_6BN

---

[*] Corresponding author: pinzhenjia@hnu.edu.cn
[†] Corresponding author: wuxingzhou@hnu.edu.cn

monolayer not only has a direct gap semiconductor but also inherits the excellent properties of graphene such as high carrier mobility, attractive optical properties, and high mechanical strength [14–16]. Compared to metal-based semiconductors, C_6BN consisting of only nonmetal *p*-block elements has the advantages of high stability, low cost, and mild toxicity [17], indicating substantial potential value for metal-free two-dimensional (2D) photocatalysts due to its good reducing ability [18]. Moreover, the pristine C_6BN could be used to detect various volatile organic compounds since the acceptor and donor behavior of B and N atoms, and the molecule-sensing performance could be further enhanced by defect or doping engineering [19,20]. Meanwhile, C_6BN is also found as a promising anode material for Li-ion [12] and K-ion batteries due to high specific capacities and low diffusion barriers [21]. The highly appealing physical properties of C_6BN motivate the search for new 2D $h-C_xB_yN_z$ materials. Most recently, Seo *et al.* [22] have successfully prepared BC_2N nanosheets by the chemical vapor deposition method. Subsequent theoretical investigations reveal that the C_2BN monolayer is also semiconducting with a similar bandgap (2.19 eV) as that of C_6BN combined with high thermal transport and mechanical properties. Zhang *et al.* [23] reported the experimentally prepared C_2BN quantum dots (QDs) have good crystallinity and semiconducting nature with an optical bandgap of 2.15 eV. In addition, they further fabricated C_2BN QD-based nonvolatile memory with superior stability and high ON/OFF ratio ($>1.74 \times 10^3$). In short, the investigation of C_6BN and C_2BN materials offers valuable insights into creating 2D semiconductors with low density, exceptional flexibility, and strong thermal conductivity, which also compensates the drawbacks of graphene and h-BN.

Understanding the thermal transport properties of the 2D $h-C_xB_yN_z$ materials composing the functional devices is a crucial process for controlling the heat dissipation in practical device applications. On the other hand, the structural diversity of 2D $h-C_xB_yN_z$ provides a natural platform to study the fundamental physics of phonon transport in low-dimensional systems. As a representative case, graphene monolayer has shown exceptional in-plane thermal conductivities ranging from 2000 to 5000 $\mathrm{W\,m^{-1}\,K^{-1}}$ [24–28], which makes graphene a promising material for thermal regulation applications. Moreover, the construction of $h-C_xB_yN_z$ superlattice was expected to stimulate the coherent interference of phonons enabling the manipulation of long-wavelength phonon transport [29,30]. It is well known that both boron and nitrogen are neighboring elements of carbon with comparable atomic sizes and a tendency to form strong covalent bonds among each other. The formation of a strong covalent network, light atomic mass, and absence of porosity in 2D ternary $h-C_xB_yN_z$ lattices are expected to correlate with their high thermal conductivity. Based on molecular dynamics simulations, Lin *et al.* [31] found that the zigzag- and armchair-oriented thermal conductivities of the C_2BN monolayer reach 806.5 and 386.1 $\mathrm{W\,m^{-1}\,K^{-1}}$ at room temperature, respectively. Meanwhile, the results obtained from the Boltzmann transport equation (BTE) indicated that the thermal conductivity of the C_2BN monolayer along different lattice directions approaches 1000 $\mathrm{W\,m^{-1}\,K^{-1}}$ [32,33]. Likewise, Mortazavi [16] reported the thermal conductivity of the C_6BN monolayer is approximately half that of graphene, because the presence of boron-nitrogen chains increases the scattering of phonons. Even so, the predicted thermal conductivity value for the C_6BN monolayer still outperforms almost all other semiconducting 2D materials. It is worthy to note that this work also indicated that the flexural acoustic (ZA) modes are the dominant heat carriers in the C_6BN monolayer and the optical modes contribute 14% and 18% to the total thermal conductivity along the armchair and zigzag directions, respectively, which is in striking contrast to the previous study where optical phonons make a notable contribution to the overall thermal conductivity [34]. The discrepancy between different simulated results is considerably related to the selection of potential functions and the ignorance of four-phonon scattering in BTE calculations, as suggested by Yang *et al.* [35]. More importantly, despite great efforts devoted to predicting the thermal conductivity of such $h-C_xB_yN_z$ structures, thermal transport in the C_6BN and C_2BN monolayers is still not well understood. Moreover, most previous predictions based on the three-phonon theory indicated that the acoustic phonons provide major contributions to the heat conduction in 2D materials. It is well known that considering only three-phonon scattering leads to significantly overestimated thermal conductivity. Thus, two important questions are naturally raised: (1) How much does the four-phonon scattering influence the thermal conductivities of the C_6BN and C_2BN monolayers? (2) How does four-phonon scattering change the role of optical phonons in these materials?

In this work, combining first-principles calculations with the BTE, we performed a comprehensive study of the fundamental lattice vibrational spectra in C_6BN and C_2BN monolayers and determined their thermal conductivity with four-phonon scattering included. It is found that four-phonon scattering can be more important than three-phonon scattering in these 2D materials as it diminishes ZA phonon thermal transport by breaking certain selection rules. Moreover, the C_6BN monolayer exhibits unusual behavior that after considering four-phonon scattering, the relative contribution of optical phonons to thermal conductivity increases to ~60% at room temperature, which differs from the traditional case where acoustic phonons dominate thermal conductivity. Such unusual phonon transport property of C_6BN can be ascribed to the fact that four-phonon scattering has a more significant impact on acoustic phonons than on optical phonons, especially ZO (out-of-plane optical) branches. Furthermore, the phonon-level systematic analysis is also carried out to understand the mechanism of the unexpected large contributions from optical phonons to thermal transport in C_6BN. This work helps deepen the understanding of thermal transport in 2D $h-C_xB_yN_z$ materials, which will benefit the applications of high-performance thermal management.

II. COMPUTATIONAL METHODOLOGY

The C_6BN monolayer is a planar honeycomb structure with a space group of P-6m2, where the rectangular unit includes six C atoms, one B atom, and one N atom with a B-N bond. The lattice configuration of C_6BN can be regarded as hexagonal carbon rings connected by alternating boron and nitrogen atoms. Meanwhile, the C_2BN monolayer also has a rectangular unit cell with two C atoms, one B atom, and one N atom, and possesses *Pmm*2 symmetry. To obtain the geometry relaxed and stress-free structures, atomic positions and lattice sizes are fully optimized by setting thresholds of 0.001 eV/Å for the forces and 10^{-8} eV for the electronic self-consistency loop. A kinetic energy cutoff of 600 eV is adopted and the Brillouin zone (BZ) is sampled using $17 \times 17 \times 1$ Γ−centered k−mesh grids. To avoid image-image interactions along with out-of-plane direction, a large vacuum space of 15 Å along the z axis is set. The finite displacement method is used to extract the second-, third-, and fourth-order interatomic force constants (IFCs), and a $9 \times 3 \times 1$ ($9 \times 5 \times 1$) supercell with a Γ-centered $3 \times 3 \times 1$ k-point mesh for BZ sampling is constructed for C_6BN (C_2BN). All first-principles calculations are implemented in the Vienna *ab initio* simulation package (VASP) using the projector augmented wave method [36]. The Perdew-Burke-Ernzerhof functional within the generalized gradient approximation is chosen to treat the exchange-correlation energy [37]. Lastly, the harmonic and anharmonic IFCs are generated by the PHONOPY package [38] and the thirdorder.py/fourthorder.py script [39,40], respectively. Here, the cut-off radius for the third-/fourth-order IFCs is considered to be the tenth/fourth nearest neighbors.

Based on harmonic and anharmonic force constants, the thermal conductivity is obtained by iteratively solving the phonon BTE,

$$\kappa^{\alpha\beta} = \frac{1}{k_B T^2 \Omega N} \sum_{q\nu} f_0(f_0+1)(\hbar\omega_{q\nu})^2 v_{q\nu}^{\alpha} F_{q\nu}^{\beta}, \qquad (1)$$

where $v_{q\nu}^{\alpha}$, f_0, and $F_{q\nu} = \tau_{q\nu}^{0}(v_{q\nu} + \Delta_{q\nu})$ are, respectively, the phonon group velocity, the Bose-Einstein distribution, and the phonon population deviation from the single-mode relaxation-time approximation (RTA) at wave vector $\boldsymbol{q}$ with band index ν. As we know, there are two different phonon-phonon scattering mechanisms regarding the momentum conservation: normal (N) and umklapp (U) processes. In the U process, the phonon propagation direction is reversed, and leads to thermal resistance. By contrast, the N process affects phonon transport by redistributing the phonon modes. Under the single-mode RTA, the N process is regarded as the contributor to thermal resistance, hence significantly underestimating κ in some materials with a strong N process such as carbon-based materials [41,42]. Here, we adopt an iterative procedure [43–45] to correct the obtained κ. A q-point mesh of $61 \times 61 \times 1$ ($31 \times 31 \times 1$) is used for three-phonon (three- and four-phonon) BTE calculations. To ensure a fair comparison between C_6BN and C_2BN monolayers, their thickness is selected to be the same as the interlayer distance of graphite (3.35 Å).

III. RESULTS AND DISCUSSION

A. Crystal structure and harmonic phonon properties

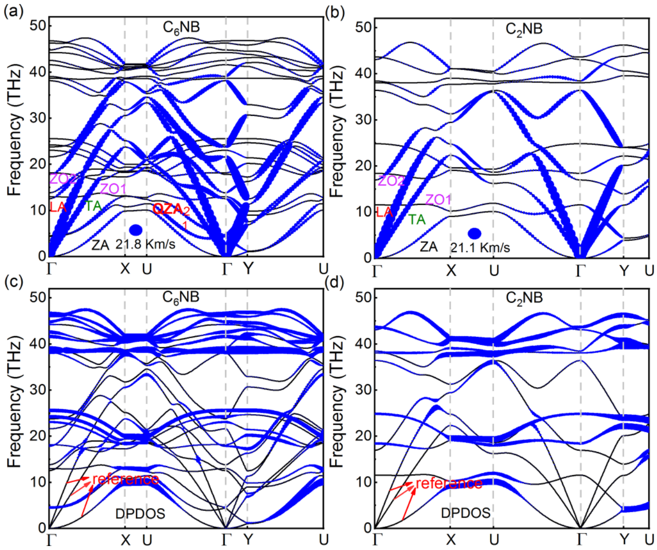

FIG. 1. Phonon dispersion along the high-symmetry q- points in the irreducible BZ with the group velocity values projected as a bubble for (a) C_6BN and (b) C_2BN, and with the DPDOS of each phonon mode projected as a bubble for (c) C_6BN and (d) C_2BN. Here, the reference value is set to 0, corresponding to the acoustic mode at the long-wavelength limit.

The optimized lattice constants of C_6BN and C_2BN are $a = 2.475$ Å, $b = 8.467$ Å and $a = 2.485$ Å, $b = 4.360$ Å, respectively, which agree well with previous theoretical results [16,32]. To identify the thermodynamic stability of these 2D h−$C_xB_yN_z$ materials, the calculated phonon dispersions are plotted in Fig. 1. Clearly, the absence of imaginary frequency in the entire BZ confirms the dynamical stability of these structures. For C_2BN, the phonon dispersion is similar to that of graphene with an orthorhombic unit cell [46], where three acoustic and nine optical phonon branches correspond to the four atoms per unit cell. Concretely, the acoustic branches include a linear longitudinal/transverse acoustic mode (labeled LA/TA) and a quadratic out-of-plane acoustic mode (labeled ZA), which is a general characteristic of 2D materials [47–50]. In addition, the lattice vibration frequency range (0–48 THz) of C_2BN is almost identical to that of graphene. In the case of C_6BN, there exist 24 phonon branches that correspond to the eight atoms in the unit cell, implying more complex phonon dispersion. An intriguing finding is that optical modes in the C_6BN lattice behave more dispersively than those in C_2BN due to more sp^2 carbon-carbon bonds, suggesting such optical modes possess higher group velocities and might contribute a significant part to heat transport. In addition, the phonon dispersion of C_6BN exhibits the parallel beam effect for the high-frequency optical branches, where two optical modes combining into a new optical mode is inhibited considerably and a high-order four-phonon scattering process is allowed [51]. Another noteworthy feature in Fig. 1(a) is that two lowest-lying out-of-plane optical branches ranging from 4 to 12 THz are well separated from the neighboring optic branches and quasiparallel to the ZA branch along the path Γ-X-U-Γ with quadratic dispersion, named QZA1 and QZA2, because they disperse very similarly to ZA modes. Actually, the quasiacoustic branches are also found in bilayer 2D materials with weak interlayer van der Waals bonding [52]. These parallel branches will restrict the three-phonon scattering channels between acoustic and optical modes (especially the ZA + ZO $\rightleftharpoons$ ZO process), because only specific reciprocal points could satisfy both momentum and energy conservation [53], resulting in a four-phonon scattering phase space

($P_4 = 1.1 \times 10^{-3}$) comparable to the value for three-phonon scattering ($P_3 = 1.3 \times 10^{-3}$). Here, the detailed calculations of P_3 and P_4 can be found in Refs. [54,55]. In contrast, the C_2BN lattice lacks the low-frequency QZA branch observed in the BC_6N monolayer. Additionally, the ZO branch in the C_2BN lattice is entangled with the LA and TA branches in the midfrequency region, which induces strong acoustic-optical interactions and facilitates a broad phase space for three-phonon scattering.

From Fig. 1, it is also seen that the ZA branch is more dispersive along the Γ-X and Γ-U paths than that along the G-Y path. This is because phonon transport has a direct interaction with BN chains in the armchair (G-Y) direction. To quantitatively elucidate the discrepancy of lattice vibration between C_6BN and C_2BN monolayers, the phonon group velocity ($v_g = \partial\omega/\partial q$) and the difference in phonon densities of states (DPDOS) between C and BN atoms are projected onto the phonon bands along high-symmetry paths. As shown in Figs. 1(a) and 1(b), the phonon group velocity in the C_6BN monolayer presents a similar variation trend to that of the C_2BN monolayer across the entire frequency range. For instance, the group velocities of LA and TA branches along the Γ-X path for the former are 21.1 and 18.6 km/s in the long-wavelength limit, while the corresponding values for the latter are 21.8 and 19.0 km/s. Meanwhile, the group velocities of the ZA branch approach zero at the Γ point due to the quadratic nature of phonon dispersion, and gradually increase with a wave vector close to the BZ center, but are far below the values of the LA and TA branches throughout the BZ. The parallel QZA1 and QZA2 branches also exhibit a similar behavior. Considering that the ZA phonons contribute the most to the thermal conductivity (κ) in numerous 2D plane materials [27,28,51], the group velocity is not the determining factor for κ in such 2D lattices. To further understand the inherent nature of the phonon spectra, the DPDOS for the C and BN domains of each vibration mode is depicted in Figs. 1(c) and 1(d). One can see that the values of the DPDOS for acoustic modes are roughly equal to 0 (as a reference point) because all atoms are vibrating in the same phase and with equal displacements, which corresponds to straight phonon transport channels. By contrast, the DPDOS for the majority of optical modes exhibits a significant deviation from the reference value, particularly within the high-frequency range. That is, the spatial distribution of vibrational spectra within the entire unit cell exhibits significant nonuniformity, indicating the presence of alloy scattering. The deviation arises from the fact that the BN chains possess a bonding configuration that differs from that of the original graphene, resulting in a more localized behavior of the vibrational states. This partially elucidates the structure-property relationship of the two graphenelike structures, specifically in relation to phonon-derived properties. However, more insight is required to reveal the phonon properties. Here, the local density of states (LDOS) at three typical frequencies of 2.08, 12.89, and 38.68 THz are depicted in Fig. 2. Clearly, the low-frequency ZA mode distributes homogeneously in the C_6BN and C_2BN lattices, and the heat carried by the acoustic phonon can flow through the system smoothly. For the medium- and high-frequency ZO modes, the vibrational states exist in certain atoms, indicating characteristic of localized modes with low group velocities (corresponding to little contribution to κ). So the potential role of low-lying QZA modes with highly dispersive features in phonon transport is curious.

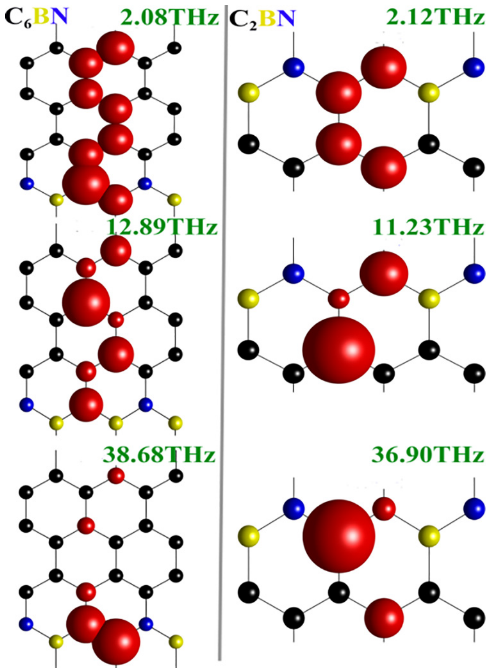

FIG. 2. The LDOS of three distinct out-of-plane phonon modes, characterized by frequencies of 2.08, 12.89, and 38.68 THz at q point (0.25, 0.0, 0.0) along the Γ-X path, which correspond to a low-frequency ZA mode, a medium-frequency ZO mode, and a high-frequency ZO mode, respectively. The highest (lowest) value is denoted by the size of the red ball.

B. Lattice thermal conductivity

Next, we examine the κ of C_6BN and C_2BN monolayers based on the BTE within the framework of RTA and iterative transport equation (ITE). As shown in Fig. 3, the calculated κ with only three-phonon scattering for the two materials exhibits significant anisotropy. Concretely, the room-temperature κ values of the C_6BN monolayer under

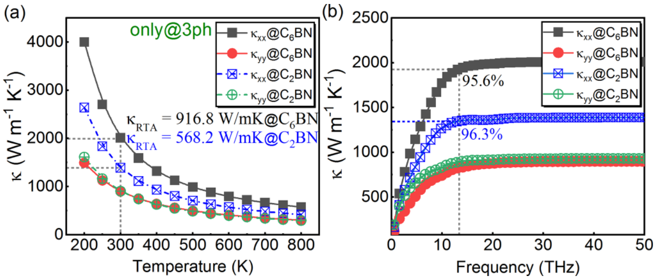

FIG. 3. The lattice thermal conductivities of C_6BN and C_2BN monolayers as a function of temperature based on both the solution of ITE and of RTA. (b) The cumulative κ as a function of frequency for the two structures. The acoustic phonon range (<14 THz) is marked by the gray-dotted line.

the ITE solution are 2008.8 W m^{-1} K^{-1} along the x axis and 897.6 W m^{-1} K^{-1} along the y axis, agreeing well with the previous result by Mortazavi *et al.* [16]. For the C$_2$BN monolayer, the κ values in both directions are 1388.4 and 904.3 W m^{-1} K^{-1}, respectively. This observation contrasts with the isotropic thermal conductivity observed in graphene [56]. The anisotropy ratio ($\gamma = \kappa_{xx}/\kappa_{yy}$) is 2.2 for the C$_6$BN monolayer and 1.5 for the C$_2$BN monolayer, which is comparable/superior to that of phosphorene (2.0) [57] but lower than that of carbon foams [58]. Moreover, the value of γ slightly decreases as temperature (T) increases. When $T =$ 800 K, it is reduced to 1.9 for the C$_2$BN monolayer. Normally, the anisotropic thermal transport behavior stems from the orientation-dependent phonon group velocity that is also indicative of the crystal structure anisotropy, as illustrated in Figs. 1(c) and 1(d). Another notable feature in Fig. 3 is that the κ of the C$_6$BN monolayer is significantly higher than that of its C$_2$BN counterpart, which is intuitively attributed to a high graphene component that facilitates the heat transport, particularly along the zigzag direction. In fact, the thermal conductivity of the C$_6$BN monolayer is quite high, compared to other semiconducting 2D materials. Furthermore, the RTA solution estimates the κ of the C$_6$BN monolayer to be 916.8 W m^{-1} K^{-1}, which is more than 50% lower than the iterative κ, implying a strong phonon hydrodynamic effect in such system. A similar behavior is present in the C$_2$BN monolayer. The aforementioned phenomenon can be explained in that the RTA solution mistakenly attributes the normal scattering process as the important factor contributing to thermal resistance, which underestimates the thermal resistance value in materials with a pronounced normal scattering process [27,59]. However, the discrepancy of obtained κ between the two solutions gradually decreases as T increases, because more high-frequency phonons are excited at high temperature and the umklapp process dominates the phonon-phonon scattering.

In addition to the overall κ, the cumulative κ with respect to frequency is calculated to ascertain the predominant frequency range in which phonons contribute significantly to phonon transport. As can be seen in Fig. 3(b), there is a slight difference between the cumulative κ of the C$_6$BN and C$_2$BN monolayers except for the amplitude. The κ value of C$_6$BN monolayer saturates at a phonon frequency of 12.8 THz (the upper limit of the QZA branch). In other words, the acoustic and low-lying optical phonons are the major carriers of heat in the C$_6$BN monolayer, which will be focused on in the following discussions. It is worth noting that the average phonon group velocities for the C$_6$BN monolayer exhibit slight differences compared to those of the C$_2$BN monolayer, and that is insufficient to account for the disparity in their thermal conductivities. Hence, other quantities such as phonon scattering rates or phonon population should be further considered.

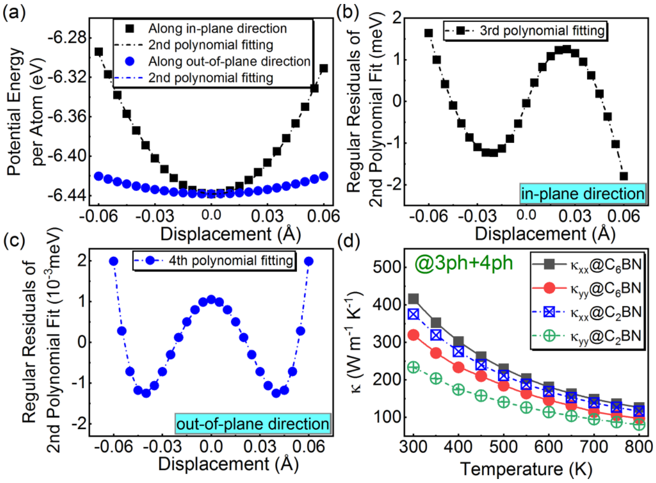

FIG. 4. (a) Potential energy versus displacement perturbation along the in-plane and out-of-plane directions for the C$_2$BN monolayer. (b) and (c) The corresponding regular residual analysis of the second polynomial fit to the potential energy curves in (a). (d) The lattice thermal conductivities of the C$_6$BN and C$_2$BN monolayers versus temperature including three-phonon scattering as well as four-phonon scattering along the zigzag (xx) and armchair (yy) directions.

The above discussion is based on the framework of the three-phonon scattering theory. Recent advances in theoretical methodologies and experimental measurements have demonstrated that the effect of four-phonon scattering on phonon transport is non-negligible not only for low thermal conductivity materials like cubic perovskites [60] but also for high thermal conductivity materials like BAs [61]. For instance, Lindsay *et al.* reported that the reflection symmetry selection rule forbids the three-phonon processes that involve an odd number of ZA modes [62], while the four-ZA processes are not restrained by the rule, as verified by Feng and Ruan [63]. Thus, a natural question arises: what is the impact of four-phonon scattering on the thermal conductivity of h$-$C$_x$B$_y$N$_z$ materials? To understand the influence of quartic anharmonicity on the obtained κ, we examined the potential energy change of N atoms moving in the in-plane/out-of-plane direction for the C$_6$BN monolayer, because the potential energy change trend of the C and B atoms is similar to that of the N atoms. By carrying out the second (2nd) polynomial fitting to the potential energy curves, we present the corresponding regular residual analysis (RRA) in Figs. 4(b) and 4(c). Through RRA, we can see that the residual shape is $\sim$ [Fig. 4(b)] when N atoms move along the in-plane direction, suggesting weak quartic anharmonicity. However, as N atoms move along the out-of-plane direction, the change in potential energy presents harmonic characteristics, and the observed residual shape is W-like [Fig. 4(c)], indicating the fourth-order term is significant and the effect of four-phonon scattering cannot be ignored in the graphenelike structures [64–66]. For this, we add the fourth-order IFCs to solve the BTE, and apply the RTA level scheme to cope with four-phonon scattering rates because the current method cannot involve a four-phonon scattering phase space iteratively. As shown in Fig. 4(d), the calculated κ values with four-phonon scattering are compared with those without the four-phonon term for the C$_6$BN and C$_2$BN monolayers, where an anticorrelation between κ and T is observed due to the intrinsic enhancement of phonon-phonon scattering versus temperature. The inclusion of four-phonon scattering suppresses κ^{3ph} by approximately 77% at room temperature, and the corresponding values are reduced from 2008.8 and 1380.5 W m^{-1} K^{-1} to 465.3 and 314.7 W m^{-1} K^{-1}, respectively. The significant reduction of thermal conductivity caused by the four-phonon scattering

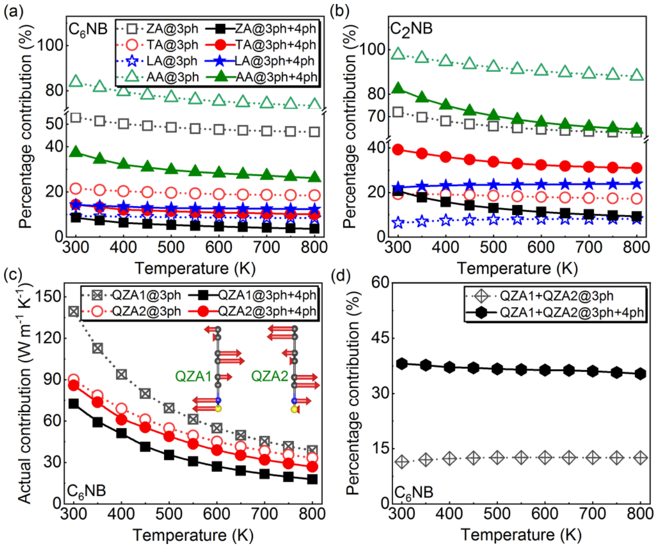

FIG. 5. Normalized contribution of three acoustic branches to the total thermal conductivity along the *xx* direction as a function of temperature for the (a) C_6BN monolayer and the (b) C_2BN monolayer. (c) The modewise thermal conductivity for the QZA1 and QZA2 phonons and (d) the sum of them to κ as a function of temperature. Dashed and solid lines represent the results excluding and including four-phonon scattering, respectively.

process has also been reported in 2D Penta-NiN2 [67], and 3D Cu_2GeSe_3 [68], which can be ascribed to the introduction of four-phonon scattering allowing for more phonon scattering channels that are not captured in three-phonon processes. Furthermore, the thermal anisotropy ratios of the C_6BN and C_2BN monolayers are little influenced by four-phonon scattering, suggesting a possible scheme for achieving directional control of thermal transport. Notably, although the κ value of the C_6BN monolayer is not as large as that in BAs and diamond [69], it still exceeds 400 W m^{-1} K^{-1} and is generally comparable with the current industrial standard for high thermal conductivity (on the bias of copper). Here, the availability of the C_6BN monolayer with ternary compound, complicated lattice structure, high thermal conductivity, and moderate direct bandgaps is quite restricted, which shows the potential for utilizing such monolayer in the development of advanced electronic and thermal management devices.

C. The role of QZA modes and mode-dependent scattering rates

To gain insight into the significant reduction of κ induced by four-phonon scattering, the percentage of contributions of different acoustic branches (ZA, TA, LA) to the x axis κ and the summation of the three terms (AA) are plotted in Fig. 5. It is clear from this graph that with only three-phonon scattering considered, the ZA modes dominate the phonon transport and the TA (LA) modes only contribute around 21.5% (9.3%) in the C_6BN monolayer at room temperature. For the C_2BN monolayer, the ZA modes contribute more than 70% and the TA (LA) modes contribute 19.3% (6.4%) to κ. This result is consistent with previous work for graphene where the ZA modes contribute ~75% to κ at 300 K [62], but differs from a 2D buckled structure like pentasilicene [70].

In the y-axis direction, the circumstances are nearly identical (not shown for brevity). The dominant contribution of the ZA modes in the 2D planar structure stems from the reflection symmetry restricting the phase space for the three-phonon scattering of ZA modes, resulting in much longer relaxation times. Moreover, the contribution of AA gradually decreases with increasing temperature, because optical phonons are activated at high temperatures. However, acoustic phonons still completely dominate the κ.

After including the four-phonon scattering, this reduction mainly comes from the ZA branch, whose thermal conductivity is reduced from 1064.6 (995.7) to 35.8 (77.6) W m^{-1} K^{-1} for the C_6BN (C_2BN) monolayer. The decreased magnitude is much larger than that in graphene (from $\kappa_{ZA}^{3ph} = 2260$ to $\kappa_{ZA}^{3\text{ and }4ph} = 235\ \mathrm{Wm^{-1}K^{-1}}$) [63]. It can be explained that the selection rules forbid certain three-phonon scattering processes, and four-phonon scattering is important in the 2D planar structure. Meanwhile, the percentage of contributions of other acoustic branches for the two monolayers exhibit quite different behaviors. Concretely the contributions of the TA and LA branches increase to around 40% and 20% in the C_2BN monolayer at room temperature, respectively, whereas those in the C_6BN monolayer decrease to around 14%. Interestingly, in the C_6BN monolayer, the optical modes exhibit an abnormal contribution (~60%) to κ, thereby disrupting the conventional dominance of acoustic modes in the phonon transport mechanism. In contrast, the contribution of optical modes in the C_2BN monolayer is found to be less than 20% of the total, similar to the findings in graphene [27] and layered Li_2ZrCl_6 [71]. It is worth mentioning that previous predictions based on the three-phonon scattering showed that optical phonons play a more significant role than acoustic phonons in determining the κ of AlSb [72,73]. However, after considering four-phonon scattering, it was found that the optical modes make little contribution to the κ, which were ascribed to the large four-phonon scattering phase space of optical phonons with flat dispersions [35]. By comparison, the presence of four-phonon scattering significantly enhances the influence of optical phonons on phonon transport in the C_6BN monolayer. This observation is not limited to the C_6BN monolayer alone, but can also be extrapolated to other 2D material systems that exhibit similar phonon-dispersion characteristics.

To understand the role of the four-phonon scattering in the unusual behavior of optical phonons, the contributions to κ from the QZA1 and QZA2 phonons are given in Fig. 5(c). Here, according to the atomic vibration information near the Γ point [the insets of Fig. 5(c)], the QZA1 mode is dominated by graphene atoms vibrating out of- phase, indicating the formation of localized states, and the QZA2 mode is dominated by both graphene and h-BN atoms vibrating out of phase, which is conducive to reduce the phonon scattering. From Fig. 5(c), it can be seen that if only the three-phonon process is considered, the contributions of the QZA1 and QZA2 phonons are 139.7 and 90.1 W m^{-1} K^{-1}, respectively, and the corresponding ratio of these values is 11.6%. Meanwhile, four-phonon scattering lowers the contribution of the QZA1 phonons from 139.7 to 73.6 W m^{-1} K^{-1}, representing a nearly 50% decrease, indicating the substantial influence of the scattering mechanism on optical phonons. Also, the contribution from the QZA2 branch is barely affected by four-phonon scattering. In this case, the contribution ratio of the QZA1 and QZA2 phonons at 300 K increases from 11.5% to 38.6%, and is insensitive to the temperature variation. As a result, the κ of the C_6BN monolayer is primarily governed by optical phonons ($\sim$60%) based on the four-phonon scattering theory, and acoustic phonons have a relatively low contribution to κ. This phenomenon can be elucidated by considering the following two factors. First, the C_6BN monolayer has a large lattice constant along the y axis ($b/a \sim 4$). In this case, the QZA1 and QZA2 branches, spanning a frequency range of 4–12 THz, can be conceptualized as folded ZA bands originating from the underlying 2D structures. This folding effect results in their group velocities being comparable to those of the acoustic branches. Despite these folded modes, other optical modes have a lower contribution to phonon transport due to a large scattering rate and low group velocity. Second, the QZA1 and ZA branches are quasiparallel and very close along the $X-U$-Γ and $Y-U$ paths. Consequently, any QZA1 phonon can readily combine with another ZA phonon and create new ZA and QZA1 phonons through the four-phonon recombination process, because the energy conservation is automatically satisfied and the conservation of momentum is easy to fulfill [53]. In comparison, the three-phonon scattering is limited because only specific reciprocal points can satisfy both momentum and energy conservation. The QZA2 branch deviates significantly from the ZA branch and lies approximately halfway between the ZA and ZO branches, showing more dispersion (see Fig. 1). For such dispersive phonon branch, the conservation of energy and momentum is more readily achieved during three-phonon processes, implying that the conventional three-phonon scattering is more prominent than four-phonon scattering for the QZA2 branch.

To gain a deeper understanding of four-phonon scattering, the phonon-isotope, three-phonon and four-phonon scattering rates versus frequency profiles of the C_6BN and C_2BN monolayers are displayed in Fig. 6. At first glance, the phonon scattering rates for different scattering mechanisms increase by several orders of magnitude (10^{-5}–10^{1} ps^{-1}) with increasing frequency. Here, the significance of phonon-isotope scattering is not as pronounced as anharmonic phonon-phonon scattering in the low-frequency range (<14 THz) at 300 K. However, it should not be disregarded entirely, because the scattering rates of optical phonons due to isotope effects are comparable to the three- and four-phonon scattering rates, especially at high temperature. The result agrees with the Yang *et al.* finding in bulk GaN [35] but differs from cubic Cu_4TiSe_4 [74] and BP [75]. Another noticeable feature in Fig. 6 is that the four-phonon scattering rates could be comparable to or even larger than the three-phonon counterparts in some frequency ranges at 300 K. Specifically, the scattering rates of the ZA and ZO phonons (in the low-frequency range of 0–14 THz) due to the quartic anharmonicity are much larger than those due to the cubic anharmonicity, which contrasts with recent investigations where the influence of four-phonon scattering on acoustic modes is smaller than optical modes [76,77]. A similar effect has been found in 2D CBN and C_4BN biphenylene [78]. The reason for this is that the reflection symmetry of planar 2D materials forbids the three-ZA scattering, but allows the four-ZA scattering, which causes high four-phonon scattering rates, even much higher than the three-phonon scattering rates at room temperature. On the other hand, the parallel ZA and ZO branches prevent ZO + ZA $\rightleftharpoons$ ZO/ZA scattering as well as the reverse process since only specific reciprocal points can satisfy both momentum conservation and energy conservation simultaneously. Nevertheless the four-phonon scattering of ZO + ZA $\rightleftharpoons$ ZO + ZA along a specific q path like $Y-U$ and U-Γ paths is less affected by the parallel configuration [53]. Considering the significant role played by these modes in phonon transport within the framework of three-phonon scattering, it is not unexpected that the inclusion of four-phonon scattering leads to a substantial suppression of κ. Moreover, the existence of intermediate-frequency ZO branches is close to the LA and TA branches, which enlarges the three-phonon scattering phase space for acoustic and optical phonons, suggesting that the three- and four-phonon resonances are equally important in the frequency region. When temperature reaches 700 K, we find that for both C_6BN and C_2BN monolayers, the four-phonon scattering rates are nearly overlapped with and even larger than the three-phonon scattering rates, as depicted in Figs. 6(b) and 6(d). This is because the three-phonon scattering exhibits a positive correlation with T, whereas the four-phonon counterparts roughly follow the scaling relation T^2 [26]. The aforementioned findings underscore the importance of four-phonon scattering in the determination of thermal conductivity for planar 2D materials. To gain more details about the four-phonon scattering processes, we plot the available scattering channels (namely, splitting, redistribution, and combination processes) for the C_6BN monolayer in Fig. 7(a). From the perspective of energy conservation during the four-phonon scattering, the combination processes primarily involve low-frequency phonons, whereas the splitting processes are primarily relevant for phonons with high energies [76]. It is important to note that the scattering rates of the recombination process, which could more easily satisfy energy conservation due to the existence of quasiparallel ZA

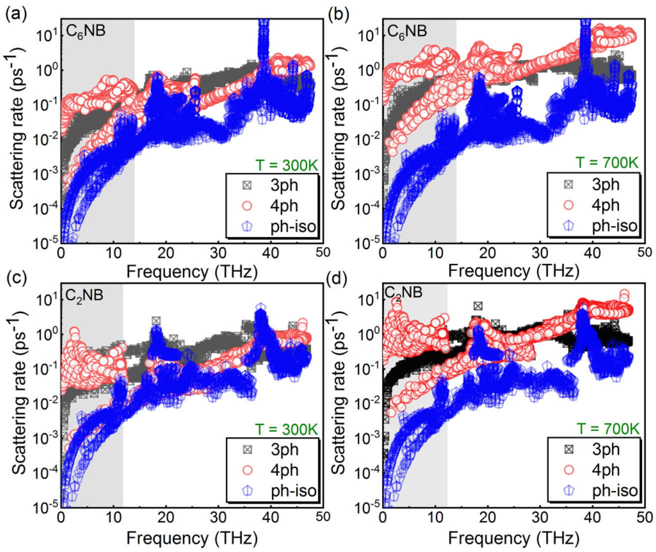

FIG. 6. The isotope-, three- and four-phonon scattering rates of the C_6BN/C_2BN monolayer at (a)/(b) 300 K and (c)/(d) 700 K. Here, the gray stripe denotes the frequency range of the ZA and QZA branches.

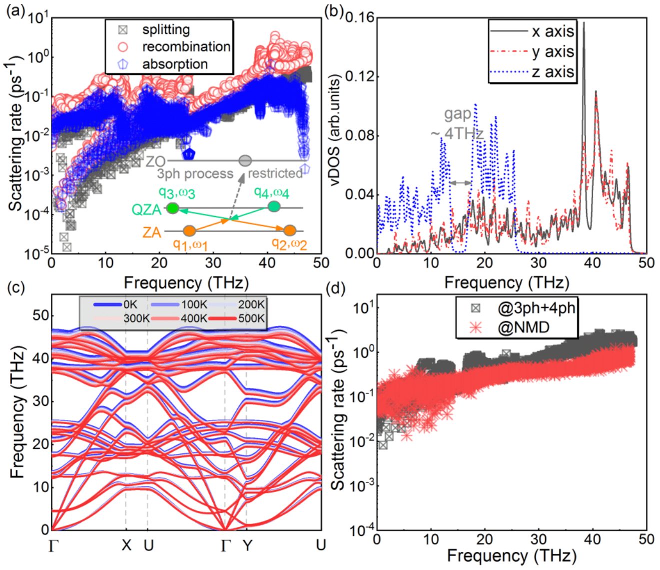

FIG. 7. (a) The contribution to four-phonon scattering rates from all allowed scattering channels at 300 K. Here, the inserted schematic diagram showing the four-phonon recombination process facilitated by the parallel ZA and QZA branches. In comparison, the three-phonon scattering process is restricted by the conservation of momentum and energy. (b) The in-plane and out-of-plane vDOS of the C_6BN monolayer at 300 K. (c) Temperature-dependent phonon dispersion of the C_6BN monolayer. (d) Comparison of the calculated scattering rates from the BTE method including three-phonon and four-phonon interactions and from (MD) simulations at 300 K.

and QZA branches [see the schematic diagram in Fig. 7(a)], are greater than those of the recombination and splitting processes. As a result, the recombination process dominates both the scattering phase space and the scattering rates [78,79]. Furthermore, the phonon vibrational density of state (vDOS) of the C_6BN monolayer along the in-plane (x and y axis) and out-of-plane (z axis) directions is examined based on *ab initio* molecular dynamics simulations. As shown in Fig. 7(b), the in-plane and out-of-plane vDOS have obvious differences across the entire frequency range. Specifically, in the low-frequency region, the population of out-of-plane vibrational modes is significantly higher compared to in-plane modes, and the scattering rate of four-phonon processes involving out-of-plane modes is considerably larger than that of other processes. Simultaneously, there is a large bandgap (∼4 THz) between the ZO1 and ZO2 branches, suggesting that ZO2 and other high-lying ZO branches are far from the QZA branch. That is, there is a reduced number of scattering channels involving QZA and high-lying ZO phonons, leading to an unusually high contribution of QZA phonons (see Fig. 5(c)).

D. Effect of phonon renormalization on phonon properties

Several recent studies have highlighted the phenomenon of temperature-induced phonon renormalization, which can lead to an upward correction in certain materials. This effect is particularly pronounced in materials with strong anharmonicity, such as Tl_3VSe_4 [80], or in materials with imaginary harmonic phonons, such as Na_2TlSb [81]. Typically, the renormalized phonons induce a significant decrease in the obtained phonon scattering rates. Here, we expect this effect to have little impact on our results, because the $h{-}C_xB_yN_z$ monolayer normally possesses high κ. To verify this hypothesis, the temperature-dependent force constants obtained by equilibrium molecular dynamics (MD) simulations (considering the effects of volumetric expansion together with the temperature-induced renormalization for the intrinsic phonon-phonon interaction) based on the moment tensor potentials (MTPs) [82] are used to extract the renormalized phonon dispersions at different temperatures. The accuracy of the MTPs potential for the C_6BN monolayer has been confirmed in a previous study [16]. As shown in Fig. 7(c), there is an apparent overlap between the LA/TA branch and the flat ZO branches in the medium-frequency region. Although the optical phonons do not make a direct contribution to κ, they can play a significant role in facilitating three-phonon scattering of the acoustic phonons responsible for heat transport (see Fig. 6). More importantly, the overall phonon spectrum exhibits minimal variation with temperature in the low-frequency range (the primary heat carriers). Meanwhile, the high-frequency modes have relatively strong negative renormalization (softened phonon) in the C_6BN monolayer, similar to that in AgI [83]. This can be explained in that the thermal expansion coefficient of graphene is known to be a negative value [84]. Hence, we believe that the effect of the temperature-induced phonon renormalization has a little effect on the calculated κ. Finally, the obtained BTE results have been validated by phonon spectral energy density (SED) analysis on the basis of MD simulations which include all high-order phonon interactions.

$$\dot{q}_{\boldsymbol{k},\nu}(t)=\sum_{\alpha}^{3}\sum_{b}^{n}\sum_{l}^{N_c}\sqrt{\frac{m_b}{N_c}}\,\dot{u}_{\alpha}^{l,b}(t)\left(e_{b,\alpha}^{\boldsymbol{k},\nu}\right)^{*}\exp\left[i\boldsymbol{k}\cdot\boldsymbol{r}_0^{l}\right], \tag{2}$$

$$\Phi_{\boldsymbol{k},\nu}(\omega)=\left|\int_{-\infty}^{+\infty}\dot{q}_{\boldsymbol{k},\nu}(t)e^{i2\pi\omega t}dt\right|^{2}. \tag{3}$$

Here, $\dot{u}_{\alpha}^{l,b}(t)$ is the α component of the velocity of atom b in the lth unit cell with equilibrium position $\boldsymbol{r}_0^l$ and $(e_{b,\alpha}^{\boldsymbol{k},\nu})^{*}$ denotes the complex conjugate of the α component for atom b of the eigenvector for mode $(\boldsymbol{k},\nu)$. The phonon scattering rates can be obtained by fitting the SED peak with the Lorentzian function.

$$\Phi_{\boldsymbol{q},\nu}(\omega)=\frac{C_{\boldsymbol{q},\nu}}{\left(\omega-\omega_{\boldsymbol{q},\nu}^{A}\right)^{2}+\Gamma_{\boldsymbol{q},\nu}^{2}}, \tag{4}$$

Where $C_{\boldsymbol{q},\nu}$ is the peak magnitude, ω is the frequency at the peak center, and $\Gamma_{\boldsymbol{q},\nu}$ is the half width at half maximum. The phonon lifetime is defined as $2\Gamma_{\boldsymbol{q},\nu}$. As shown in Fig. 7(d), for the C_6BN monolayer, the scattering rates of low-frequency phonons obtained from the two methods coincide with each other, while those of high-frequency optical modes are found to be larger from MD simulations. This discrepancy might slightly affect the validity of our calculated three- and four-phonon scattering rates since the high-lying optical phonons have less contribution to κ in the C_6BN monolayer. Here, the distinct differences seen between the high-lying optical phonon scattering rates calculated using the BTE and MD methods are probably associated with the different phonon statistics [85] and the deviations from Matthiessen's rule owing to interference effects between different scattering events [86]. Under the BTE framework, it is easy to distinguish phonon scattering contributions from different orders of the anharmonicity which are assumed to be much smaller than the harmonic phonon eigenfrequency.

IV. CONCLUSIONS

In summary, by combining first-principles calculations with the BTE, we have studied the phonon interaction and thermal conductivity in C_6BN and C_2BN monolayers. The calculated results reveal that C_6BN and C_2BN present high lattice thermal conductivities of 416.2 and 375.4 $\mathrm{W\,m^{-1}\,K^{-1}}$ at room temperature, respectively, which are substantially reduced compared to those involving only three-phonon scattering. It is found that four-phonon scattering can be more important than three-phonon scattering as it diminishes the contribution to κ from ZA phonons by breaking certain selection rules. Moreover, the C_6BN monolayer exhibits the unusual behavior that optical phonons contribute ~60% to κ under the four-phonon picture, which differs from the traditional case where acoustic phonons dominate thermal conductivity. The unusual phonon transport property of the C_6BN monolayer can be ascribed to the fact that the QZA branch possesses harmonic (high group velocity and large vDOS) and anharmonic (low scattering rates) properties, which are analogous to those found in acoustic phonons. Furthermore, the phonon-level systematic analysis is also carried out to understand the mechanism of the unexpected large contributions from optical phonons to thermal transport in the C_6BN monolayer. This finding not only highlights insight into the nature of phonon transport, but also provides a promising strategy for manipulation of heat transport based on optical phonon modes.

ACKNOWLEDGMENTS

This work was supported by the National Natural Science Foundation of China (Grants No. 12074115 and No. 11904161), by the Scientific Research Fund of Hunan Provincial Education Department (Grants No. 21B0401 and No. 22B0868), and by the National College Students Innovation and Entrepreneurship Training Program (S202310555083). The computational work was supported by the HPC Center of University of South China.

---

[1] Y. Wu, Y. M. Lin, A. A. Bol, K. A. Jenkins, F. Xia, D. B. Farmer, Y. Zhu, and P. Avouris, High-frequency, scaled graphene transistors on diamond-like carbon, Nature (London) **472**, 74 (2011).

[2] M. Liu, X. Yin, E. Ulin-Avila, B. Geng, T. Zentgraf, L. Ju, F. Wang, and X. Zhang, A graphene-based broadband optical modulator, Nature (London) **474**, 64 (2011).

[3] C. Lee, X. Wei, J. W. Kysar, and J. Hone, Measurement of the elastic properties and intrinsic strength of monolayer graphene, Science **321**, 385 (2008).

[4] Z. Yan, G. Liu, J. M. Khan, and A. A. Balandin, Graphene quilts for thermal management of high-power GaN transistors, Nat. Commun. **3**, 827 (2012).

[5] X. Dong, T. Chen, G. Liu, L. Xie, G. Zhou, and M. Long, Multifunctional 2D $g{-}C_4N_3/MoS_2$ vdW heterostructure-based nanodevices: Spin filtering and gas sensing properties, ACS Sens. **7**, 3450 (2022).

[6] Q. Liu, J. J. Li, D. Wu, X. Q. Deng, Z. H. Zhang, Z. Q. Fan, and K. Q. Chen, Gate-controlled reversible rectifying behavior investigated in a two-dimensional MoS_2 diode, Phys. Rev. B **104**, 045412 (2021).

[7] K. Watanabe, T. Taniguchi, and H. Kanda, Direct-bandgap properties and evidence for ultraviolet lasing of hexagonal boron nitride single crystal, Nat. Mater. **3**, 404 (2004).

[8] L. Ci, L. Song, C. Jin, D. Jariwala, D. Wu, Y. Li, A. Srivastava, Z. F. Wang, K. Storr, L. Balicas, F. Liu, and P. M. Ajayan, Atomic layers of hybridized boron nitride and graphene domains, Nat. Mater. **9**, 430 (2010).

[9] Y. Ni, H. Zhang, S. Hu, H. Wang, S. Volz, and S. Xiong, Interface diffusion-induced phonon localization in two-dimensional lateral heterostructures, Int. J. Heat Mass Transfer **144**, 118608 (2019).

[10] A. Kınacı, J. B. Haskins, C. Sevik, and T. Çağın, Thermal conductivity of BN-C nanostructures, Phys. Rev. B **86**, 115410 (2012).

[11] P.-Z. Jia, J.-P. Xie, X.-K. Chen, Y. Zhang, X. Yu, Y.-J. Zeng, Z.-X. Xie, Y.-X. Deng, and W.-X. Zhou, Recent progress of two-dimensional heterostructures for thermoelectric applications, J. Phys.: Condens. Matter **35**, 073001 (2023).

[12] M. Kawaguchi, Y. Imai, and N. Kadowaki, Intercalation chemistry of graphite-like layered material BC_6N for anode of Li ion battery, J. Phys. Chem. Solids **67**, 1084 (2006).

[13] K. Matsui, S. Oda, K. Yoshiura, K. Nakajima, N. Yasuda, and T. Hatakeyama, One-shot multiple borylation toward BN-doped nanographenes, J. Am. Chem. Soc. **140**, 1195 (2018).

[14] X. Liu, X. Ma, H. Gao, X. Zhang, H. Ai, W. Li, and M. Zhao, Valley-selective circular dichroism and high carrier mobility of graphene-like BC_6N, Nanoscale **10**, 13179 (2018).

[15] L. B. Shi, M. Yang, S. Cao, Q. You, Y. J. Zhang, M. Qi, K. C. Zhang, and P. Qian, Prediction of high carrier mobility for a novel two-dimensional semiconductor of BC_6N: First principles calculations, J. Mater. Chem. C **8**, 5882 (2020).

[16] B. Mortazavi, Ultrahigh thermal conductivity and strength in direct-gap semiconducting graphene-like BC_6N: A first-principles and classical investigation, Carbon **182**, 373 (2021).

[17] C. Li, Y. Xu, W. Tu, G. Chen, and R. Xu, Metal-free photocatalysts for various applications in energy conversion and environmental purification, Green Chem. **19**, 882 (2017).

[18] S. Karmakar and S. Dutta, Strain-tuneable photocatalytic ability of BC_6N monolayer: A first principle study, Comput. Mater. Sci. **202**, 111002 (2022).

[19] S. M. Aghaei, A. Aasi, S. Farhangdoust, and B. Panchapakesan, Graphene-like BC_6N nanosheets are potential candidates for detection of volatile organic compounds (VOCs) in human breath: A DFT study, Appl. Surf. Sci. **536**, 147756 (2021).

[20] Y. Yong, F. Ren, Z. Zhao, R. Gao, S. Hu, Q. Zhou, and Y. Kuang, Highly enhanced $NH_3{-}$sensing performance of BC_6N monolayer with single vacancy and Stone-Wales defects: A DFT study, Appl. Surf. Sci. **551**, 149383 (2021).

[21] P. Xiang, S. Sharma, Z. M. Wang, J. Wu, and U. Schwingenschlögl, Flexible C_6BN monolayers as promising anode materials for high-performance K-ion batteries, ACS Appl. Mater. Interfaces **12**, 30731 (2020).

[22] T. H. Seo, W. Lee, K. S. Lee, J. Y. Hwang, D. I. Son, S. Ahn, H. Cho, M. J. Kim, and M. J. Kim, Dominant formation of $h-BC_2N$ in $h-B_xC_yN_z$ films: CVD synthesis and characterization, Carbon **182**, 791 (2021).

[23] P. Zhang, C. Hou, W. Shao, R. Liu, Z. Wu, and G. Tai, Crystalline BC_2N quantum dots, Nano Res. **16**, 7837 (2023).

[24] H. Wang, S. Hu, K. Takahashi, X. Zhang, H. Takamatsu, and J. Chen, Experimental study of thermal rectification in suspended monolayer graphene, Nat. Commun. **8**, 15843 (2017).

[25] Z. Zhang, Y. Ouyang, Y. Cheng, J. Chen, N. Li, and G. Zhang, Size-dependent phononic thermal transport in low-dimensional nanomaterials, Phys. Rep. **860**, 1 (2020).

[26] X. Gu, Z. Fan, H. Bao, and C. Y. Zhao, Revisiting phonon-phonon scattering in single-layer graphene, Phys. Rev. B **100**, 064306 (2019).

[27] X. Yang, Z. Liu, F. Meng, and W. Li, Tuning the phonon transport in bilayer graphene to an anomalous regime dominated by electron-phonon scattering, Phys. Rev. B **104**, L100306 (2021).

[28] J. Chen, J. He, D. Pan, X. Wang, N. Yang, J. Zhu, S. A. Yang, and G. Zhang, Emerging theory and phenomena in thermal conduction: A selective review, Sci. China: Phys. Mech. Astron. **65**, 117002 (2022).

[29] T. Zhu and E. Ertekin, Phonon transport on two-dimensional graphene/boron nitride superlattices, Phys. Rev. B **90**, 195209 (2014).

[30] X. Wu, X. Huang, L. Yang, Z. Zhang, Y. Guo, S. Volz, Q. Han, and M. Nomura, Suppressed thermal transport in mathematically inspired 2D heterosystems, Carbon **213**, 118264 (2023).

[31] C. Lin, X. Zhang, and Z. Rao, Theoretical prediction of thermal transport in BC_2N monolayer, Nano Energy **38**, 249 (2017).

[32] B. Mortazavi, I. S. Novikov, and A. V. Shapeev, A machine-learning-based investigation on the mechanical/failure response and thermal conductivity of semiconducting BC_2N monolayers, Carbon **188**, 431 (2022).

[33] A. Shafique and Y. H. Shin, Ultrahigh and anisotropic thermal transport in the hybridized monolayer (BC_2N) of boron nitride and graphene: A first-principles study, Phys. Chem. Chem. Phys. **21**, 17306 (2019).

[34] R. Muthaiah and J. Garg, Ultrahigh thermal conductivity in hexagonal BC_6N- An efficient material for nanoscale thermal management—A first principles study, Comput. Mater. Sci. **200**, 110773 (2021).

[35] X. Yang, T. Feng, J. Li, and X. Ruan, Stronger role of four-phonon scattering than three-phonon scattering in thermal conductivity of III-V semiconductors at room temperature, Phys. Rev. B **100**, 245203 (2019).

[36] G. Kresse and J. Furthmüller, Efficient iterative schemes for *ab initio* total-energy calculations using a plane-wave basis set, Phys. Rev. B **54**, 11169 (1996).

[37] J. P. Perdew, K. Burke, and M. Ernzerhof, Generalized gradient approximation made simple, Phys. Rev. Lett. **77**, 3865 (1996).

[38] A. Togo and I. Tanaka, First principles phonon calculations in materials science, Scr. Mater. **108**, 1 (2015).

[39] W. Li, J. Carrete, N. A. Katcho, and N. Mingo, ShengBTE: A solver of the Boltzmann transport equation for phonons, Comput. Phys. Commun. **185**, 1747 (2014).

[40] Z. Han, X. Yang, W. Li, T. Feng, and X. Ruan, FourPhonon: An extension module to ShengBTE for computing four-phonon scattering rates and thermal conductivity, Comput. Phys. Commun. **270**, 108179 (2022).

[41] Y. Guo, Z. Zhang, M. Bescond, S. Xiong, M. Wang, M. Nomura, and S. Volz, Size effect on phonon hydrodynamics in graphite microstructures and nanostructures, Phys. Rev. B **104**, 075450 (2021).

[42] A. Cepellotti, G. Fugallo, L. Paulatto, M. Lazzeri, F. Mauri, and N. Marzari, Phonon hydrodynamics in two-dimensional materials, Nat. Commun. **6**, 6400 (2015).

[43] A. Chernatynskiy and S. R. Phillpot, Evaluation of computational techniques for solving the Boltzmann transport equation for lattice thermal conductivity calculations, Phys. Rev. B **82**, 134301 (2010).

[44] W. Li, N. Mingo, L. Lindsay, D. A. Broido, D. A. Stewart, and N. A. Katcho, Thermal conductivity of diamond nanowires from first principles, Phys. Rev. B **85**, 195436 (2012).

[45] A. Ward, D. A. Broido, D. A. Stewart, and G. Deinzer, *Ab initio* theory of the lattice thermal conductivity in diamond, Phys. Rev. B **80**, 125203 (2009).

[46] C. da Silva, F. Saiz, D. A. Romero, and C. H. Amon, Coherent phonon transport in short-period two-dimensional superlattices of graphene and boron nitride, Phys. Rev. B **93**, 125427 (2016).

[47] P. Z. Jia, Z. X. Xie, Y. X. Deng, Y. Zhang, L. M. Tang, W. X. Zhou, and K. Q. Chen, High thermoelectric performance induced by strong anharmonic effects in monolayer $(PbX)_2$ ($X = S$, Se, Te), Appl. Phys. Lett. **121**, 043901 (2022).

[48] Z. X. Xie, X. K. Chen, X. Yu, Y. X. Deng, Y. Zhang, W. X. Zhou, and P. Z. Jia, Intrinsic thermoelectric properties in biphenylene nanoribbons and effect of lattice defects, Comput. Mater. Sci. **220**, 112041 (2023).

[49] Y. J. Zeng, Y. X. Feng, L. M. Tang, and K. Q. Chen, Effect of out-of-plane strain on the phonon structures and anharmonicity of twisted multilayer graphene, Appl. Phys. Lett. **118**, 183103 (2021).

[50] D. Wu, L. Huang, P. Z. Jia, X. H. Cao, Z. Q. Fan, W. X. Zhou, and K. Q. Chen, Tunable spin electronic and thermoelectric properties in twisted triangulene π-dimer junctions, Appl. Phys. Lett. **119**, 063503 (2021).

[51] L. Yu, A. Chen, X. Wang, H. Wang, Z. Qin, and G. Qin, Softened sp^2-sp^3 bonding network leads to strong anharmonicity and weak hydrodynamics in graphene$^+$, Phys. Rev. B **106**, 125410 (2022).

[52] X. Zhang, X. F. Qiao, W. Shi, J. B. Wu, D. S. Jiang, and P. H. Tan, Phonon and Raman scattering of two-dimensional transition metal dichalcogenides from monolayer, multilayer to bulk material, Chem. Soc. Rev. **44**, 2757 (2015).

[53] L. Xie, J. H. Feng, R. Li, and J. Q. He, First-principles study of anharmonic lattice dynamics in low thermal conductivity $AgCrSe_2$: Evidence for a large resonant four-phonon scattering, Phys. Rev. Lett. **125**, 245901 (2020).

[54] L. Lindsay and D. A. Broido, Three-phonon phase space and lattice thermal conductivity in semiconductors, J. Phys.: Condens. Matter **20**, 165209 (2008).

[55] X. Yang, T. Feng, J. Li, and X. Ruan, Evidence of fifth-and higher-order phonon scattering entropy of zone-center optical phonons, Phys. Rev. B **105**, 115205 (2022).

[56] L. F. C. Pereira and D. Donadio, Divergence of the thermal conductivity in uniaxially strained graphene, Phys. Rev. B **87**, 125424 (2013).

[57] S. Lee, F. Yang, J. Suh, S. Yang, Y. Lee, G. Li, H. S. Choe, A. Suslu, Y. Chen, C. Ko, J. Park, K. Liu, J. Li, K. Hippalgaonkar, J. J. Urban, S. Tongay, and J. Wu, Anisotropic in-plane thermal conductivity of black phosphorus nanoribbons at temperatures higher than 100 K, Nat. Commun. **6**, 8573 (2015).

[58] X. K. Chen, X. Y. Hu, P. Jia, Z. X. Xie, and J. Liu, Tunable anisotropic thermal transport in porous carbon foams: The role of phonon coupling, Int. J. Mech. Sci. **206**, 106576 (2021).

[59] X. K. Chen, X. Y. Hu, P. Z. Jia, and G. F. Xie, First-principles determination of high thermal conductivity of PCF-graphene: A comparison with graphene, Appl. Phys. Lett. **121**, 182205 (2022).

[60] Y. Zhao, S. Zeng, G. Li, C. Lian, Z. Dai, S. Meng, and J. Ni, Lattice thermal conductivity including phonon frequency shifts and scattering rates induced by quartic anharmonicity in cubic oxide and fluoride perovskites, Phys. Rev. B **104**, 224304 (2021).

[61] J. S. Kang, M. Li, H. Wu, H. Nguyen, and Y. Hu, Experimental observation of high thermal conductivity in boron arsenide, Science **361**, 575 (2018).

[62] L. Lindsay, D. A. Broido, and N. Mingo, Flexural phonons and thermal transport in graphene, Phys. Rev. B **82**, 115427 (2010).

[63] T. Feng and X. Ruan, Four-phonon scattering reduces intrinsic thermal conductivity of graphene and the contributions from flexural phonons, Phys. Rev. B **97**, 045202 (2018).

[64] S. Yue, X. Zhang, G. Qin, S. Phillpot, and M. Hu, Metric for strong intrinsic fourth-order phonon anharmonicity, Phys. Rev. B **95**, 195203 (2017).

[65] S. Bi, Z. Chang, K. Yuan, Z. Sun, X. Zhang, Y. Gao, and D. Tang, First-principles prediction of the lattice thermal conductivity of two-dimensional (2D) h-BX (X = P, As, Sb) considering the effects of fourth-order and all-order scattering, J. Appl. Phys. **132**, 114301 (2022).

[66] X. Wu, V. Varshney, J. Lee, T. Zhang, J. L. Wohlwend, A. K. Roy, and T. Luo, Hydrogenation of penta-graphene leads to unexpected large improvement in thermal conductivity, Nano Lett. **16**, 3925 (2016).

[67] C. Zhang, J. Sun, Y. Shen, W. Kang, and Q. Wang, Effect of high order phonon scattering on the thermal conductivity and its response to strain of a penta-NiN_2 sheet, J. Phys. Chem. Lett. **13**, 5734 (2022).

[68] H. Shao, D. Ding, Y. Fang, W. Song, J. Huang, C. Dong, and H. Zhang, Phonon transport in Cu_2GeSe_3: Effects of spin-orbit coupling and higher-order phonon-phonon scattering, Phys. Rev. B **107**, 085202 (2023).

[69] X. Qian, J. Zhou, and G. Chen, Phonon-engineered extreme thermal conductivity materials, Nat. Mater. **20**, 1188 (2021).

[70] Z. Gao, Z. Zhang, G. Liu, and J. S. Wang, Ultra-low lattice thermal conductivity of monolayer penta-silicene and penta-germanene, Phys. Chem. Chem. Phys. **21**, 26033 (2019).

[71] C. W. Wu, X. Ren, S. Y. Li, Y. J. Zeng, W. X. Zhou, and G. Xie, Significant regulation of stress on the contribution of optical phonons to thermal conductivity in layered Li_2ZrCl_6: First-principles calculations combined with the machine-learning potential approach, Appl. Phys. Lett. **121**, 172201 (2022).

[72] L. Lindsay, D. A. Broido, and T. L. Reinecke, *Ab initio* thermal transport in compound semiconductors, Phys. Rev. B **87**, 165201 (2013).

[73] N. K. Ravichandran and D. Broido, Phonon-phonon interactions in strongly bonded solids: Selection rules and higher-order processes, Phys. Rev. X **10**, 021063 (2020).

[74] X. K. Chen, E. M. Zhang, D. Wu, and K. Q. Chen, Strain-induced medium-temperature thermoelectric performance of Cu_4TiSe_4: The role of four-phonon scattering, Phys. Rev. Appl. **19**, 044052 (2023).

[75] G. Li, Q. Wang, Z. Cui, and R. Guo, Competition between intrinsic and extrinsic phonon scatterings in cubic BP and BAs with point defects, Phys. Rev. B **107**, 184118 (2023).

[76] Y. Xia, V. I. Hegde, K. Pal, X. Hua, D. Gaines, S. Patel, J. He, M. Aykol, and C. Wolverton, High-throughput study of lattice thermal conductivity in binary rocksalt and zinc blende compounds including higher-order anharmonicity, Phy. Rev. X **10**, 041029 (2020).

[77] P. H. Du, C. Zhang, T. Li, and Q. Sun, Low lattice thermal conductivity with two-channel thermal transport in the superatomic crystal PH_4AlBr_4, Phys. Rev. B **107**, 155204 (2023).

[78] F. Lv, H. Liang, and Y. Duan, Funnel-shaped electronic structure and enhanced thermoelectric performance in ultralight $C_x(BN)_{1-x}$ biphenylene networks, Phys. Rev. B **107**, 045422 (2023).

[79] Y. Xia and M. K. Chan, Anharmonic stabilization and lattice heat transport in rocksalt β-GeTe, Appl. Phys. Lett. **113**, 193902 (2018).

[80] Y. Xia, K. Pal, J. He, V. Ozoliņš, and C. Wolverton, Particlelike phonon propagation dominates ultralow lattice thermal conductivity in crystalline Tl_3VSe_4, Phys. Rev. Lett. **124**, 065901 (2020).

[81] T. Yue, Y. Zhao, J. Ni, S. Meng, and Z. Dai, Strong quartic anharmonicity, ultralow thermal conductivity, high band degeneracy and good thermoelectric performance in Na_2TlSb, npj Computat. Mater. **9**, 17 (2023).

[82] A. V. Shapeev, Moment tensor potentials: A class of systematically improvable interatomic potentials, Multiscale Model. Simul. **14**, 1153 (2016).

[83] Y. Wang, Q. Gan, M. Hu, J. Li, L. Xie, and J. He, Anharmonic lattice dynamics and the origin of intrinsic ultralow thermal conductivity in AgI materials, Phys. Rev. B **107**, 064308 (2023).

[84] D. Yoon, Y. W. Son, and H. Cheong, Negative thermal expansion coefficient of graphene measured by Raman spectroscopy, Nano Lett. **11**, 3227 (2011).

[85] M. Puligheddu, Y. Xia, M. Chan, and G. Galli, Computational prediction of lattice thermal conductivity: A comparison of molecular dynamics and Boltzmann transport approaches, Phys. Rev. Mater. **3**, 085401 (2019).

[86] M. Žnidarič, Modified Matthiessen's rule: More scattering leads to less resistance, Phys. Rev. B **105**, 045140 (2022).